Future changes to El Niño-Southern Oscillation temperature and precipitation teleconnections

Sarah J. Perry[1,2,3], Shayne McGregor[2,3], Alex Sen Gupta[1,3], Matthew H. England[1,3]

[1] Climate Change Research Centre, University of New South Wales Sydney

[2] School of Earth, Atmosphere and Environment, Monash University

[3] Australian Research Council Centre of Excellence for Climate System Science

Key Points

- The majority of CMIP5 models project robust increases in the spatial extent of ENSO temperature and precipitation teleconnections over land.

- The increase in area is related to the amplified ENSO-driven precipitation across the equatorial Pacific in the future.

- Despite the robust increase in area over land, we do not find a consistent strengthening of these teleconnections in the individual models.

Future changes to El Niño-Southern Oscillation temperature and precipitation teleconnections

Abstract

Potential changes to the El Niño-Southern Oscillation (ENSO) resulting from climate change may have far reaching impacts through atmospheric teleconnections. Here, ENSO temperature and precipitation teleconnections between the historical and high-emission future simulations are compared in 40 models from phase 5 of the Coupled Model Intercomparison Project (CMIP5). Focusing on the global land area only, we show that there are robust increases in the spatial extent of ENSO teleconnections during austral summer in 2040-2089 of ~19% for temperature and ~12% for precipitation in the multi-model mean (MMM), relative to the 1950-1999 period. The MMM further shows the expansion of ENSO teleconnection extent is at least partly related to a strengthening of ENSO teleconnections over continental regions, however, a consistent strengthening is not found across the individual models. This suggests that while more land may be affected by ENSO, the existing teleconnections may not be simply strengthened.

Introduction

The El Niño-Southern Oscillation (ENSO) is the largest source of interannual climate variability, contributing to substantial changes in rainfall, temperature, and extreme weather around the globe. Although there are robust projections of climate change impacts for changes in the long-term average temperature and precipitation for the next century (*IPCC*, 2014), there remains uncertainty around how the characteristics of ENSO and its teleconnections may change in the future (*Collins et al*., 2010), despite models showing an increase in the frequency of extreme ENSO events (*Cai et al.,* 2015). The uncertainty arises from the different representations of the coupled ocean and atmosphere feedback processes that control ENSO, with the CMIP5 models showing no clear consensus on whether ENSO sea surface temperature (SST) variability will increase or decrease (*Watanabe et al.,* 2012; *Guilyardi et al.,* 2009; *Stevenson et al.,* 2012).

Despite the lack of agreement in projected changes to ENSO SST variability, recent studies have shown that there is a consistent projected strengthening of the atmospheric response to ENSO across the equatorial Pacific. *Power et al*. (2013) show that for ENSO SST anomalies (SSTAs) of the same structure and magnitude, anomalous convection is greater in the 21st century compared to the 20th century due to background warming in the equatorial Pacific. They further show that the nonlinear contribution to intensified precipitation from background warming can be enhanced or damped by projected changes in ENSO variance and structural changes to ENSO SSTAs, which have less intermodel agreement. *Cai et al.* (2014) also show that the faster rates of warming projected for the equatorial and eastern Pacific reduces the zonal and meridional gradients of SST, increasing the frequency of deep convection anomalies including the southward shift of the intertropical convergence zone which signifies extreme El Niño events.

The enhanced thermodynamic response in the central and eastern Pacific is the result of the interaction between the warmer and moister atmosphere (*Huang and Xie*, 2015; *Held and Soden*, 2006) and the total SST arising from ENSO SSTAs superimposed upon the mean warming of the equatorial Pacific (*Johnson and Xie*, 2010), forming conditions that are more conducive to deep convection and contributing to an eastward shift of the convective heating anomaly (*Power et al.,* 2013; *Cai et al*., 2014). As the latent heat release from anomalous deep convection is the driving mechanism of atmospheric teleconnections that cause the remote impacts of ENSO (*Hoskins and Karoly*, 1981; *Chiang and Sobel*, 2002; *Trenberth et al., 1999*), it follows that increases in ENSO-driven convection in the tropical Pacific may cause changes in ENSO teleconnections to remote regions (*Watanabe et al*., 2014).

Recent model studies have begun to provide insight into potential changes to ENSO teleconnections. Using atmosphere-only models, *Zhou et al*. (2014) show that the eastward shift of deep convection during El Niño combined with mean warming drives a strengthened Pacific North America (PNA) teleconnection pattern, intensifying the ENSO-driven precipitation variability across North America. This is also consistent with other studies which suggest geographical changes in ENSO teleconnections, the magnitude of which depend on both external forcing and ENSO amplitude changes (e.g. *Stevenson,* 2012*; Kug et al*. 2010; *Meehl and Teng,* 2007). For example, in a global study, *Bonfils et al*. (2015) project the observed pattern of ENSO variability onto CMIP5 model output from the historical and RCP8.5 simulations to obtain a “typical” ENSO SST pattern and associated precipitation teleconnections for the current and future climates. They find intensified ENSO-driven precipitation in the future simulations, and show that this increase in precipitation response is modulated by the projected change in the amplitude of ENSO variability in each model (*Bonfils et al*., 2015). To date, there has been limited research investigating future changes in temperature teleconnections, or examining in detail changes over land where ENSO events have the greatest societal impacts. Here we expand upon the analysis of *Power et al*. (2013) by examining a larger ensemble of CMIP5 models, and broadening the focus from the equatorial Pacific Ocean to identify the changes in ENSO-driven variability that occur over remote land areas.

Methods

2.1 Data

We analyse monthly precipitation and surface temperature output from 40 CMIP5 models (see *Taylor et al.*, 2012; Supplementary Table 1). We compare the ENSO teleconnections simulated in different climate conditions over two fifty-year periods: between 1950-1999 in the historical simulations, and between 2040-2089 in the high-emissions RCP8.5 simulations, where anthropogenic radiative forcing reaches 8.5 W m^2 by 2100. For models that have archived multiple historical and RCP8.5 simulations, we use output from the first ensemble member only. The data processing and identification of the ENSO signal follows *Power et al.* (2013). Surface temperature and precipitation data are interpolated to a 1.5° latitude by 1.5° longitude grid and a high-pass spectral filter is applied to remove variability with a period greater than 13 years including the climatological mean, global warming signal and any multidecadal variability. Subsequent analysis focuses on the austral summer season, December-February (DJF), when ENSO variability peaks. For comparison with observed ENSO teleconnections, we analyse observations of temperature from the NCEP/NCAR reanalysis (*Kalnay et al.,*1996) for a comparable fifty-year period between 1953-2002, and precipitation from the CMAP dataset (*Xie and Arkin*, 1997) between 1984-2010, applying the same temporal filtering outlined above. The first and last five years of the datasets are discarded to minimise edge effects introduced by the spectral filter.

2.2 Identifying ENSO and ENSO teleconnections

Following *Power et al*. (2013), ENSO patterns for models and observations observations were calculated using an Empirical Orthogonal Function (EOF) analysis of the equatorial ocean domain (30°S-30°N, 0-360°E). The first EOF of both the equatorial ocean SST and precipitation represents the ENSO mode, with its associated principle component (PC) illustrating the temporal evolution of El Niño and La Niña events. Separate EOFs were calculated for each model for each 50-year time period, and for both SST and precipitation, to identify if structural changes in ENSO or ENSO's teleconnections are apparent. The first PCs for temperature and precipitation are highly correlated for each model with an ensemble median correlation of 0.94 (interquartile range (IQR) of 0.91-0.97) for the historical period. The ENSO signal is insensitive to the zonal domain: the correlation between the first PC for the equatorial ocean and the equatorial Pacific Ocean exceeds 0.98 for the majority of models.

To identify global ENSO teleconnection patterns, the normalised SST and precipitation PCs were linearly regressed against the respective global surface temperature or precipitation filtered time series at all locations. The resulting regression maps (Figure 1) illustrates the mean change in temperature or precipitation (in degrees Celsius or millimetres per day) at each grid point that is associated with a one standard deviation change in the ENSO PC. The strongest relationships are expected over the equatorial Pacific Ocean, the source of ENSO variability, with significant ($p < 0.05$) regressions elsewhere indicative of remote ENSO teleconnections. The proportion of global land area having a significant regression is hereafter referred to as the spatial extent of the ENSO teleconnections. We further test where there is agreement across the model ensemble in the location of significant ENSO teleconnections. When at least 25 out of the 40 models show a statistically significant regression with ENSO at a given location the level of intermodel agreement (62.5%) is considered significant at $p < 0.1$ based on a binomial distribution (*Power et al*., 2012), assuming that each model is an independent sample (*Annan and Hargreaves*, 2017). Regions that meet this requirement for intermodel agreement are hereafter referred to as having a significant MMM teleconnection.

Results

3.1 Comparison to observed ENSO teleconnections

Previous studies have shown that the CMIP5 models are capable of simulating the dynamics of ENSO with varying degrees of fidelity (e.g. *Bellenger et al.,* 2014; *Taschetto et al*., 2014; *Weare*, 2013). Comparison of the multi-model mean (MMM) teleconnection maps from the historical period with the observed teleconnection maps (Figure 1), indicates that the MMM captures the broad-scale observed ENSO teleconnections. The spatial correlation between the MMM temperature teleconnection for the historical period and the observed teleconnection for all land areas is 0.61. Significant ($p < 0.05$) observed temperature teleconnections cover 36.2% of the global land area (stippling in Figure 1a). This is within the range of the individual CMIP5 models and is similar to the median spatial extent of 37.0% (IQR of 30.2-47.0%) (Supplementary Table 1). However, only 17.4% of the global land area has a significant MMM teleconnection (where at least 25 out of 40 models agree, corresponding to $p < 0.1$). This area is shown by the stippling in Figure 1c, and includes parts of northern South America, Central Africa, the Maritime Continent and northern Australia. Despite the broad similarity of the observed and MMM teleconnection, the spatial correlation between the observed and simulated temperature teleconnections over land in the individual models is relatively low, with an ensemble median of 0.34 (IQR of 0.22-0.50).

The spatial correlation between the MMM precipitation teleconnection map for the historical period and the observed teleconnection map for the global land area is 0.56. This is again considerably higher than the spatial correlation between the observed and simulated precipitation teleconnections over land for most individual models, which have a median correlation of 0.38 (IQR of 0.30-0.44). The spatial extent of the observed precipitation teleconnection is smaller than the temperature teleconnection, covering 23.5% of the global land area (stippling in Figure 1b). This observed area of significant teleconnections over land falls in the lower range of the individual model spread, where the median percentage of land with a significant precipitation teleconnection is 26.4% (IQR of 18.9-32.7%) (Supplementary Table 1). As with temperature, the models show limited agreement in the locations where ENSO teleconnections are significant, with a significant MMM teleconnection covering only 3.12% of the global land area for precipitation (stippling in Figure 1d).

For both temperature and precipitation, the limited intermodel agreement in the MMM teleconnections, and the low spatial correlation when compared to the observed teleconnections, are influenced by: i) the differences in the individual models representation of ENSO SSTAs and subsequently its teleconnections (*Bellenger et al*., 2013; *Taschetto et al*., 2014; *Weare,* 2013); and ii) stochastic noise arising from the use of relatively short fifty-year time periods to derive the ENSO teleconnections (*Batehup et al*., 2015; *Wittenberg*, 2009). The effect of the short record is further discussed in Section 3.2.

3.2 Global changes to ENSO teleconnections

We now focus on how ENSO teleconnections over land are projected to change subject to continued high emissions as per the RCP8.5 simulations. The spatial similarities between the 1950-1999 and 2040-2089 periods are clear from the MMM teleconnection maps (Figure 1c-f), as reflected by the spatial correlation over land of 0.95 for both temperature and precipitation. Despite the similarity of the MMM patterns, the median spatial correlation for the global land area across the models between the two periods is 0.44 (IQR of 0.32-0.67) for temperature, and 0.69 (IQR of 0.54-0.80) for precipitation. To examine if the projected changes in the teleconnection patterns are a result of external forcing or internal variability, we compare the spatial correlations of DJF ENSO teleconnection maps for an ensemble of simulations from two models, HadGem2-ES and CCSM4 (Supplementary Table 2 and 3). We seek to determine if the range of spatial correlations over land between the historical and future simulations in these models lies outside the range of stochastic variability sampled between model ensemble members during the historical period. To this end, a two-sample t-test was calculated between the two distributions (historical-historical versus historical-future) for each model and for temperature and precipitation. Three of the four comparisons revealed correlations between the historical and future teleconnections that were not statistically different ($p < 0.05$) from comparison within the historical period itself. This suggests that the stochasticity of the climate system is likely to have a strong influence on the low spatial correlation in individual ensemble members, and as such it will be hard to separate from any forced signal.

To further examine whether changes are occurring in ENSO teleconnections over land, we calculate the change in area of significant teleconnections between the two time periods. Examining the models individually, we find that the land area with significant ENSO temperature teleconnections increases in 28 out of 40 models (Figure 2a; Supplementary

Table 1). This level of model agreement is significant above the 99% level ($p < 0.01$) based on a binomial distribution. For the individual models, the mean change in spatial extent is 10.15% (IQR of -5.68 to 26.6%) (Supplementary Table 1), relative to the 1950-1999 period, and is significantly different from 0 ($p < 0.05$) using a t-test. The land area with a significant MMM teleconnection (where at least 25 out of 40 models agree, corresponding to $p < 0.1$) increases by approximately 19% in the 2040-2089 period, relative to the 1950-1999 period. This is most prominent over equatorial Africa, South America and Australia (Figure 1c and e).

For precipitation, the land area with a significant precipitation teleconnection is also increasing in 27 out of 40 models (Figure 2b; Supplementary Table 1), with an equivalent significance level of $p < 0.02$ based on a binomial distribution. The mean change over land in the individual models, relative to the 1950-1999 period, is 5.93% (IQR of -3.70 to 14.5%) (Supplementary Table 1), however this change is not significant ($p < 0.05$) using a t-test. The area with a significant precipitation teleconnection in the MMM similarly shows an increase in the future period, although the change is smaller than that found for temperature. The increase in the land area with a significant MMM teleconnection is approximately 12% relative to the 1950-1999 period, and primarily occurs over equatorial Africa and South America, including an area over northern Chile that is significant in the future period only (Figure 1d and f).

To determine if this change in ENSO teleconnections is seasonally dependent, we repeat our analysis for the other seasons (MAM, JJA, SON), and for an annual average calculated between July and June of the following year. The spatial extent of significant teleconnections in the MMM and individual models differs with the seasons for both temperature and precipitation (Supplementary Figure 1). However, the spatial extent of significant temperature teleconnections over land for the individual models is increasing for all seasons and the annual average. The level of intermodel agreement for the increase in area is significant above the 90% level ($p < 0.1$) in all cases (Supplementary Figure 1). In contrast, the precipitation teleconnection is found to have significant intermodel agreement ($p < 0.02$) on the increase in the area of significant teleconnections over land for DJF only (Supplementary Figure 1). For the annual average and all other seasons there is no significant agreement across the ensemble in the change in teleconnections over land for precipitation.

3.3 Relationship to changes in ENSO variance

We next examine whether the projected change in teleconnection spatial extent is dependent on the change in ENSO variability to determine if those models with enhanced (suppressed) ENSO variability in the future simulations also have increased (decreased) ENSO teleconnections. We compare the change in area of significant ENSO teleconnections to the change in standard deviation of the SSTA in the Niño 3.4 region (190-240°E, 5°S-5°N), calculated using high-pass filtered DJF means for each model. The change in standard deviation between the two time periods was normalised by the historical standard deviation for each model to illustrate the proportional change in variability relative to the models initial ENSO variability. Figure 3 (a and b) shows that there is a significant ($p < 0.05$) intermodel relationship between the change in ENSO variability and the change in the area of significant ENSO teleconnections during DJF for both temperature and precipitation, suggesting that part of the change in teleconnection area can be associated with changes in ENSO variability in the future. For example, each model with enhanced ENSO variability also shows an increase in the temperature teleconnection spatial extent, but not all the models with reduced

ENSO variability show decreases in spatial extent. This contributes to the positive offset of the regression model, which suggests that models displaying no change in ENSO variability will on average display an increase in the spatial extent of significant temperature teleconnections over land. A similar relationship is also evident for the precipitation teleconnection, however there are a few models with increased ENSO SSTA variability that also show decreasing teleconnection spatial extent (Figure 3b). Thus, the positive offsets of the regression models (Figure 3a and b) suggest an increase in the teleconnection area that is unrelated to the changes in ENSO SSTA variability.

As previous studies have shown that the precipitation response in the tropics to unchanged ENSO SSTAs is enhanced in future climate conditions (*Chung et al*., 2014; *Power et al*., 2013), we further compare the change in teleconnection area to the change in the total ENSO-driven precipitation over the equatorial Pacific Ocean. We define the change in ENSO-driven precipitation as the difference between the cumulative sum of precipitation regression coefficients over the equatorial Pacific Ocean between 120-290°E, 10°S-10°N (c.f. Figure 1d and f). A significant ($p < 0.05$) intermodel relationship is found for the change in ENSO-driven precipitation and teleconnection area for both temperature and precipitation (Figure 3c and d). For temperature, the majority of models show increased (decreased) teleconnections associated with increased (decreased) ENSO-driven precipitation, with the change in ENSO-driven precipitation explaining a greater portion of the change in teleconnection area than the change in ENSO SSTA variance. Further, the positive offset is reduced, suggesting that the increased ENSO-driven precipitation response is at least partly responsible for the increased ENSO temperature teleconnections over land. However, the result is not as clear for precipitation, as although the positive offset is again slightly reduced, ENSO SSTA variance explains more of the change in precipitation teleconnections than the change in precipitation over the equatorial Pacific Ocean.

3.4 Changes to the strength of the ENSO teleconnections over land

Here we examine whether the intensity of the ENSO teleconnections over land during DJF is also strengthened in the future period. Comparison of the MMM difference between the historical and future teleconnection maps (Supplementary Figure 2) indicates that there are regions where the strength of ENSO's teleconnections, calculated as the magnitude of the regression coefficients, are projected to change. A two-sided t-test was calculated to determine if the mean of the regression coefficients for the individual models at each grid point is significantly different ($p<0.05$) between the historical and future simulations (stippling in Supplementary Figure 2). Based on regions which have a significant teleconnection in the MMM in either period, increases in the temperature teleconnection strength are evident over areas of South America, eastern and western Africa. Changes in the strength of the precipitation teleconnection are evident for central and eastern Africa (Supplementary Figure 2).

We quantify the magnitude of the change in teleconnection strength over land by comparing the difference between the regression coefficients (2040-2089 – 1950-1999) at the locations where there is a significant teleconnection in the MMM in either period (stippling in Figure 1c-f) against the historical period (Figure 4). The regression slope (0.15 +/- 0.014) indicates that the MMM temperature teleconnection at these locations is on average stronger in the future period (Figure 4a). However, the relatively low R^2 of 0.25 suggests that this strengthening is not a uniform intensification of the historical MMM temperature teleconnection over land (cf. Supplementary Figure 3a). This is also the case for the MMM precipitation teleconnection (Figure 4b), which displays a slight strengthening in the future period (0.04 +/- 0.023), while the low R^2 of 0.03 indicates little similarity between the teleconnection change and the historical teleconnection (cf. Supplementary Figure 3b). Comparing the change in teleconnection strength for the same land area as the MMM in the individual models also reveals there is no significant intermodel agreement (based on the binomial distribution) on a strengthening of the teleconnections over land (Supplementary Figure 4). This is at least partly influenced by noise in the climate system, which is reduced in the MMM, as discussed in Section 3.2. However, we do find a clear relationship between the change in each models ENSO teleconnection strength and the change in the teleconnection spatial extent over land, with larger changes in teleconnection area associated with strengthened teleconnections (Supplementary Figure 4).

4 Summary and Conclusion

Recent studies have shown a consistent projected strengthening of the atmospheric response to ENSO SSTAs across the equatorial Pacific (*Power et al*., 2013; *Cai et al*., 2014), which may enhance remote teleconnections due to the increase in latent heating (*Watanabe et al*., 2014). Our analysis shows that with future warming under the RCP8.5 simulations, the spatial extent of ENSO temperature teleconnections in the MMM (where at least 25 out of 40 models agree on the location of teleconnections, corresponding to $p < 0.1$) increases by approximately 19% in the 2040-2089 period relative to 1950-1999, and this increase is seen regardless of the season analysed. The MMM precipitation teleconnection increases in area by approximately 12%, however a significant change only occurs during DJF. Although there is spread across the individual ensemble members regarding the change in teleconnection area, we find a significant level of agreement for an increase in area amongst the individual models that is also robust when separating the models according to the teleconnection skill (Supplementary Table 1). This may have implications for reconstructions of past ENSO variability from remote proxies that assume ENSO teleconnections are stationary (*McGregor et al.,* 2013, 2010; *Li et al*., 2011, 2013).

In agreement with previous studies (*Bonfils et al*., 2015), we show that changes in the spatial extent of the ENSO teleconnections are at least partly related to the change in amplitude of SSTAs in the Niño 3.4 region. However, the amplitude changes cannot entirely explain the mean increase in the spatial extent of ENSO teleconnections over land. This is supported by the fact that approximately half of all models displaying reduced future ENSO amplitudes display an increase in the teleconnection spatial extent. We further show there is a relationship between this mean change in area and ENSO-driven precipitation across the equatorial Pacific, consistent with the suggestions of *Power et al*. (2013), *Cai et al*. (2014) and *Watanabe et al*. (2014). It is important to note that neither predictor explains more than half of the intermodel differences in the change in spatial extent, suggesting there may be additional mechanisms that contribute to this change in teleconnection area that have not yet been considered. Further exploration of the underlying mechanisms remains an avenue for future work.

For land areas where there are significant MMM teleconnections, we show that although the MMM teleconnection is strengthened in the future period this strengthening varies by location for both temperature or precipitation. Further, analysis of the individual models does not show a consistent strengthening of the teleconnection over land. As the strengthening of the future teleconnection over land areas lacks consistency across the individual models, we suggest that while the land area that is being impacted by ENSO variability is increasing, it is unlikely that the future teleconnections will simply reflect an enhancement of the historical teleconnections.

References

Annan, J. D., and J. C. Hargreaves (2017), On the meaning of independence in climate science, *Earth Syst. Dyn.*, *8*(1), 211–224, doi:10.5194/esd-8-211-2017.

Batehup, R., S. McGregor, and A. J. E. Gallant (2015), The influence of non-stationary teleconnections on palaeoclimate reconstructions of ENSO variance using a pseudoproxy framework, *Clim. Past*, *11*(12), 1733–1749, doi:10.5194/cp-11-1733-2015.

Bellenger, H., E. Guilyardi, J. Leloup, M. Lengaigne, and J. Vialard (2014), ENSO representation in climate models: From CMIP3 to CMIP5, *Clim. Dyn.*, *42*(7–8), 1999–2018, doi:10.1007/s00382-013-1783-z.

Bonfils, C. J. W., B. D. Santer, T. J. Phillips, K. Marvel, L. Ruby Leung, C. Doutriaux, and A. Capotondi (2015), Relative contributions of mean-state shifts and ENSO-driven variability to precipitation changes in a warming climate, *J. Clim.*, *28*(24), 9997–10013, doi:10.1175/JCLI-D-15-0341.1.

Cai, W. et al. (2014), Increasing frequency of extreme El Niño events due to greenhouse warming, *Nat. Clim. Chang.*, *5*(2), 1–6, doi:10.1038/nclimate2100.

Cai, W. et al. (2015), ENSO and greenhouse warming, *Nat. Clim. Chang.*, *5*(9), 849–859, doi:10.1038/nclimate2743.

Chiang, J. C. H., and A. H. Sobel (2002), Tropical tropospheric temperature variations caused by ENSO and their influence on the remote tropical climate, *J. Clim.*, *15*(18), 2616–2631, doi:10.1175/1520-0442(2002)015<2616:TTTVCB>2.0.CO;2.

Chung, C. T. Y., S. B. Power, J. M. Arblaster, H. A. Rashid, and G. L. Roff (2014), Nonlinear precipitation response to El Nino and global warming in the Indo-Pacific, *Clim. Dyn.*, *42*(7–8), 1837–1856, doi:10.1007/s00382-013-1892-8.

Collins, M. et al. (2010), The impact of global warming on the tropical Pacific ocean and El Nino, *Nat. Geosci.*, *3*(6), 391–397, doi:10.1038/ngeo868

Guilyardi, E., A. Wittenberg, A. Fedorov, M. Collins, C. Wang, A. Capotondi, G. J. van Oldenborgh, and T. Stockdale (2009), Understanding El Niño in ocean-atmosphere general circulation models: Progress and challenges, *Bull. Am. Meteorol. Soc.*, *90*(3), 325–340, doi:10.1175/2008BAMS2387.1.

Held, I. M., and B. J. Soden (2006), Robust responses of the hydrologic cycle to global warming, *J. Clim.*, *19*, 5686–5699, doi:10.1175/JCLI3990.1.

Hoskins, B. J., and D. J. Karoly (1981), The Steady Linear Response of a Spherical Atmosphere to Thermal and Orographic Forcing, *J. Atmos. Sci.*, *38*(6), 1179–1196, doi:10.1175/1520-0469(1981)038<1179:TSLROA>2.0.CO;2.

Huang, P., and S.-P. Xie (2015), Mechanisms of change in ENSO-induced tropical Pacific rainfall variability in a warming climate, *Nat. Geosci.*, *8*(October), 1–13, doi:10.1038/ngeo2571.

IPCC, 2014. *Climate Change 2014: Synthesis Report. Contribution of Working Groups I, II and III to the Fifth Assessment Report of the Intergovernmental Panel on Climate Change* [Core Writing Team, R.K. Pachauri and L.A. Meyer (eds.)]. IPCC, Geneva, Switzerland, 151pp.

Johnson, N. C., and S. P. Xie (2010), Changes in the sea surface temperature threshold for tropical convection, *Nat. Geosci.*, *3*(12), 842–845, doi:Doi 10.1038/Ngeo1008.

Kalnay, E. et al. (1996), The NCEP/NCAR 40-Year Reanalysis Project, *Bull. Am. Meteorol. Soc.*, *77*(3), 437–471, doi:10.1175/1520-0477(1996)077<0437:TNYRP>2.0.CO;2.

Kug, J. S., S. Il An, Y. G. Ham, and I. S. Kang (2010), Changes in El Niño and La Niña teleconnections over North Pacific-America in the global warming simulations, *Theor. Appl. Climatol.*, *100*(3), 275–282, doi:10.1007/s00704-009-0183-0.

Li, J., S.-P. Xie, E. R. Cook, G. Huang, R. D'Arrigo, F. Liu, J. Ma, and X.-T. Zheng (2011), Interdecadal modulation of El Niño amplitude during the past millennium, *Nat. Clim. Chang.*, *1*(2), 114–118, doi:10.1038/nclimate1086.

Li, J. et al. (2013), El Niño modulations over the past seven centuries, *Nat. Clim. Chang.*, *3*(9), 822–826, doi:10.1038/nclimate1936.

McGregor, S., A. Timmermann, and O. Timm (2010), A unified proxy for ENSO and PDO variability since 1650, *Clim. Past*, *6*, 1–17, doi:10.5194/cpd-5-2177-2009.

McGregor, S., A. Timmermann, M. H. England, O. Elison Timm, and A. T. Wittenberg (2013), Inferred changes in El Niño-Southern Oscillation variance over the past six centuries, *Clim. Past*, *9*(5), 2269–2284, doi:10.5194/cp-9-2269-2013.

Meehl, G. A., and H. Teng (2007), Multi-model changes in El Nino teleconnections over North America in a future warmer climate, *Clim. Dyn.*, *29*(7–8), 779–790, doi:10.1007/s00382-007-0268-3.

Power, S. B., F. Delage, R. Colman, and A. Moise (2012), Consensus on twenty-first-century rainfall projections in climate models more widespread than previously thought, *J. Clim.*, *25*(11), 3792–3809, doi:10.1175/JCLI-D-11-00354.1.

Power, S., F. Delage, C. Chung, G. Kociuba, and K. Keay (2013), Robust twenty-first-century projections of El Niño and related precipitation variability., *Nature*, *502*(7472), 541–5, doi:10.1038/nature12580.

Stevenson, S. L. (2012), Significant changes to ENSO strength and impacts in the twenty-first century: Results from CMIP5, *Geophys. Res. Lett.*, *39*(17), 1–6, doi:10.1029/2012GL052759.

Stevenson, S., B. Fox-Kemper, M. Jochum, R. Neale, C. Deser, and G. Meehl (2012), Will There Be a Significant Change to El Niño in the Twenty-First Century?, *J. Clim.*, *25*(6), 2129–2145, doi:10.1175/JCLI-D-11-00252.1.

Taschetto, A. S., A. Sen Gupta, N. C. Jourdain, A. Santoso, C. C. Ummenhofer, and M. H. England (2014), Cold tongue and warm pool ENSO Events in CMIP5: Mean state and future projections, *J. Clim.*, *27*(8), 2861–2885, doi:10.1175/JCLI-D-13-00437.1.

Taylor, K. E., R. J. Stouffer, and G. A. Meehl (2012), An overview of CMIP5 and the experiment design, *Bull. Am. Meteorol. Soc.*, *93*(4), 485–498, doi:10.1175/BAMS-D-11-00094.1.

Trenberth, K. E., G. W. Branstator, D. Karoly, A. Kumar, N. C. Lau, and C. Ropelewski (1998), Progress during TOGA in understanding and modeling global teleconnections associated with tropical sea surface temperatures, *J. Geophys. Res.*, *103*(C7), 14291–14324, doi:10.1029/97jc01444.

Watanabe, M., J-S. Kug, F-F. Jin, M. Collins, M. Ohba, and A.T. Wittenberg (2012), Uncertainty in the ENSO amplitude change from the past to the future, *Geophys. Res. Lett.*, 1-6, doi:10.1029/2012GL053305.

Watanabe, M., Y. Kamae, and M. Kimoto (2014), Robust increase of the equatorial Pacific rainfall and its variability in a warmed climate, *Geophys. Res. Lett.*, 1–6, doi:10.1002/2014GL059692.

Weare, B. C. (2013), El Nino teleconnections in CMIP5 models, *Clim. Dyn.*, *41*(7–8), 2165–2177, doi:10.1007/s00382-012-1537-3.

Wittenberg, A. T. (2009), Are historical records sufficient to constrain ENSO simulations?, *Geophys. Res. Lett.*, *36*(12), 1–5, doi:10.1029/2009GL038710.

Xie, P. P., and P. A. Arkin (1997), Global precipitation: A {17-year} monthly analysis based on gauge observations, satellite estimates, and numerical model outputs, *Bull. Amer.*

Meteor. Soc., *78*(11), 2539–2558, doi:10.1175/1520-0477(1997)078<2539:GPAYMA>2.0.CO;2.

Zhou, Z. Q., S. P. Xie, X. T. Zheng, Q. Liu, and H. Wang (2014), Global warming-induced changes in El Nino teleconnections over the North Pacific and North America, *J. Clim.*, *27*(24), 9050–9064, doi:10.1175/JCLI-D-14-00254.1.

Acknowledgements

We acknowledge the World Climate Research Programme's Working Group on Coupled Modelling and the climate modelling groups listed in Supplementary Table 1 for producing and making available CMIP5 model output. This research was supported by the Australian Research Council (ARC) including the ARC Centre of Excellence in Climate System Science. We would also like to thank the two reviewers for their constructive feedback.

Figure 1: Regression of normalised ENSO index (defined in Section 2.2) on global surface temperature and precipitation. (a) NCEP/NCAR Reanalysis temperature observations (1953-2002), (b) CMAP precipitation observations (1984-2010), (c, d) MMM historical simulations (1950-1999), (e, f) MMM RCP8.5 simulations (2040-2089). Stippling in a and b shows significant regressions at $p < 0.05$. Stippling in c-f shows significant teleconnections in the MMM (where 25 out of 40 models agree on the location of significant teleconnections, corresponding to a significance level of $p < 0.1$).

Figure 2: Percentage of the global land area that has a significant regression with ENSO ($p < 0.05$) for the historical and future periods in each model for (a) temperature and (b) precipitation. The relationship between the two time periods for the ensemble is given by the regression equation *y* (solid red line) including the upper and lower 95% confidence intervals for the slope (dashed red lines). Reference numbers correspond to models given in Supplementary Table 1. The blue line indicates the percentage of land with a significant ENSO teleconnection in the observations. The grey dashed line illustrates the 1:1 line.

Figure 3: The relationship between the change in teleconnection spatial extent over land versus the change in ENSO variability. In (a, b) ENSO variability is the change in standard deviation of the Niño3.4 region SSTAs, (c, d) the change in the total sum of the precipitation regression coefficients over the tropical Pacific Ocean (120-290°E, 10°S-10°N). The regression relationship for the ensemble is shown by equation *y* (solid red lines) including the upper and lower 95% confidence intervals for the slope (dashed red lines). Reference numbers correspond to models given in Supplementary Table 1.

Figure 4: The relationship between the change in teleconnections (future-historical MMM regression coefficients) and the historical teleconnections for land areas where there is a significant teleconnection in the MMM (where 25 out of 40 models agree on the location of significant teleconnections, corresponding to a significance level of $p < 0.1$), for (a) temperature and (b) precipitation. Each point represents a land grid point that is significant in the MMM in one or both time periods. The regression relationship is given by the equation *y* (solid red lines) including the upper and lower 95% confidence intervals on the slope (dashed red lines). The grey dashed line illustrates the 1:1 line.

Figure 1.

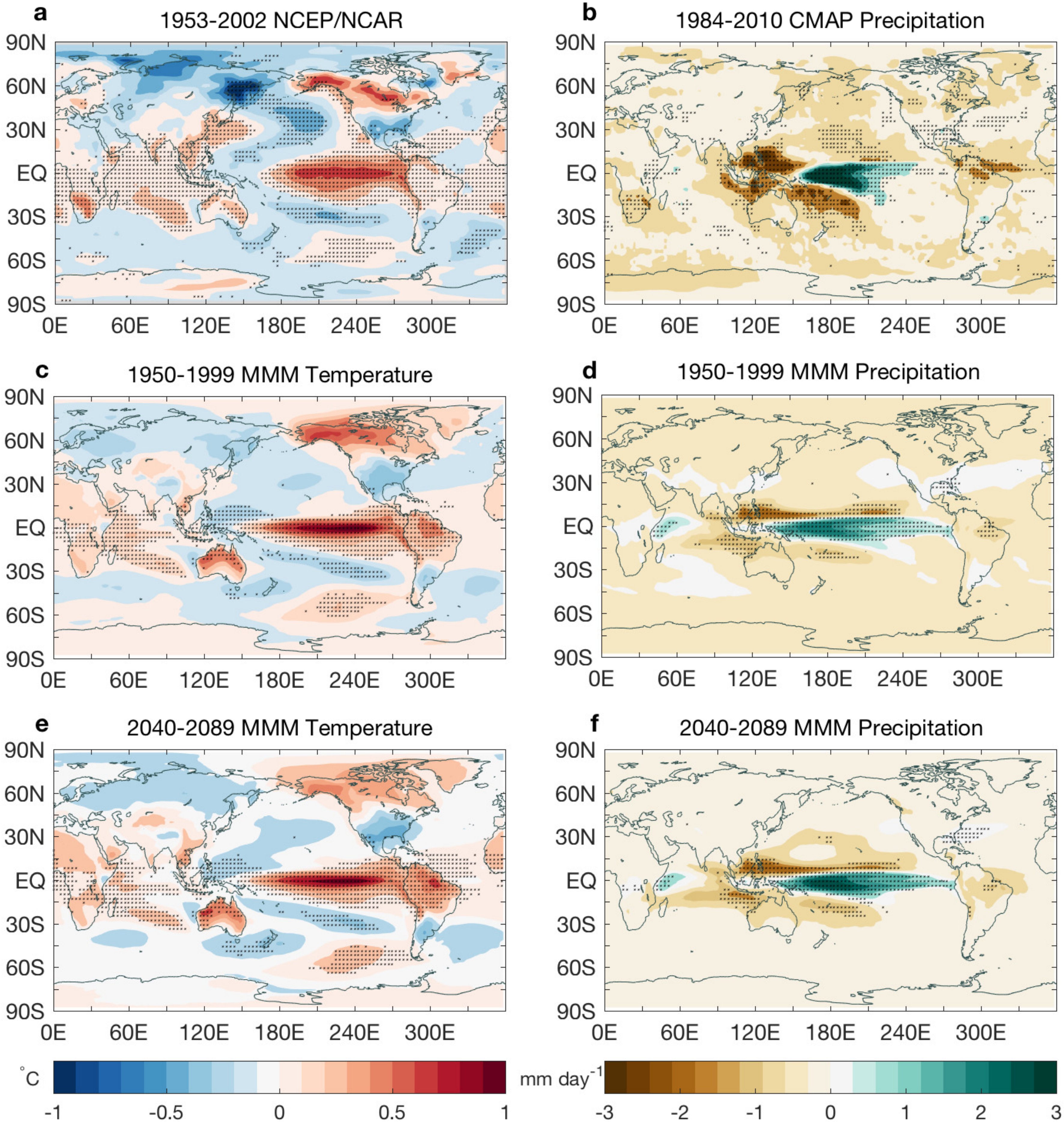

a
1953-2002 NCEP/NCAR
b
1984-2010 CMAP Precipitation
c
1950-1999 MMM Temperature
d
1950-1999 MMM Precipitation
e
2040-2089 MMM Temperature
f
2040-2089 MMM Precipitation
90N
60N
30N
EQ
30S
60S
90S
0E
60E
120E
180E
240E
300E
°C
-1
-0.5
0
0.5
1
mm day^{-1}
-3
-2
-1
0
1
2
3

Figure 2.

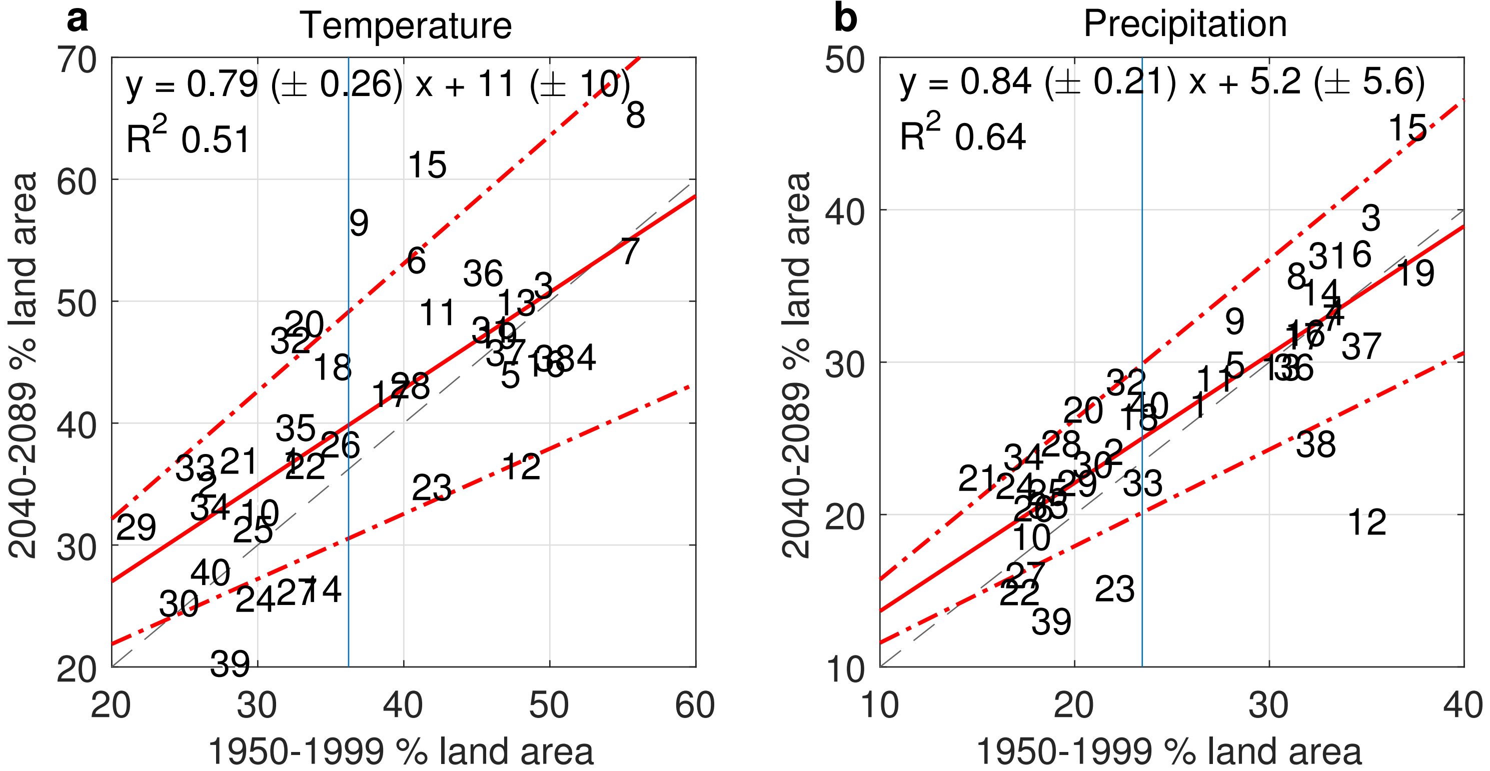
a
Temperature
y = 0.79 (± 0.26) x + 11 (± 10)
R2 0.51
2040-2089 % land area
1950-1999 % land area
b
Precipitation
y = 0.84 (± 0.21) x + 5.2 (± 5.6)
R2 0.64
2040-2089 % land area
1950-1999 % land area

Figure 3.

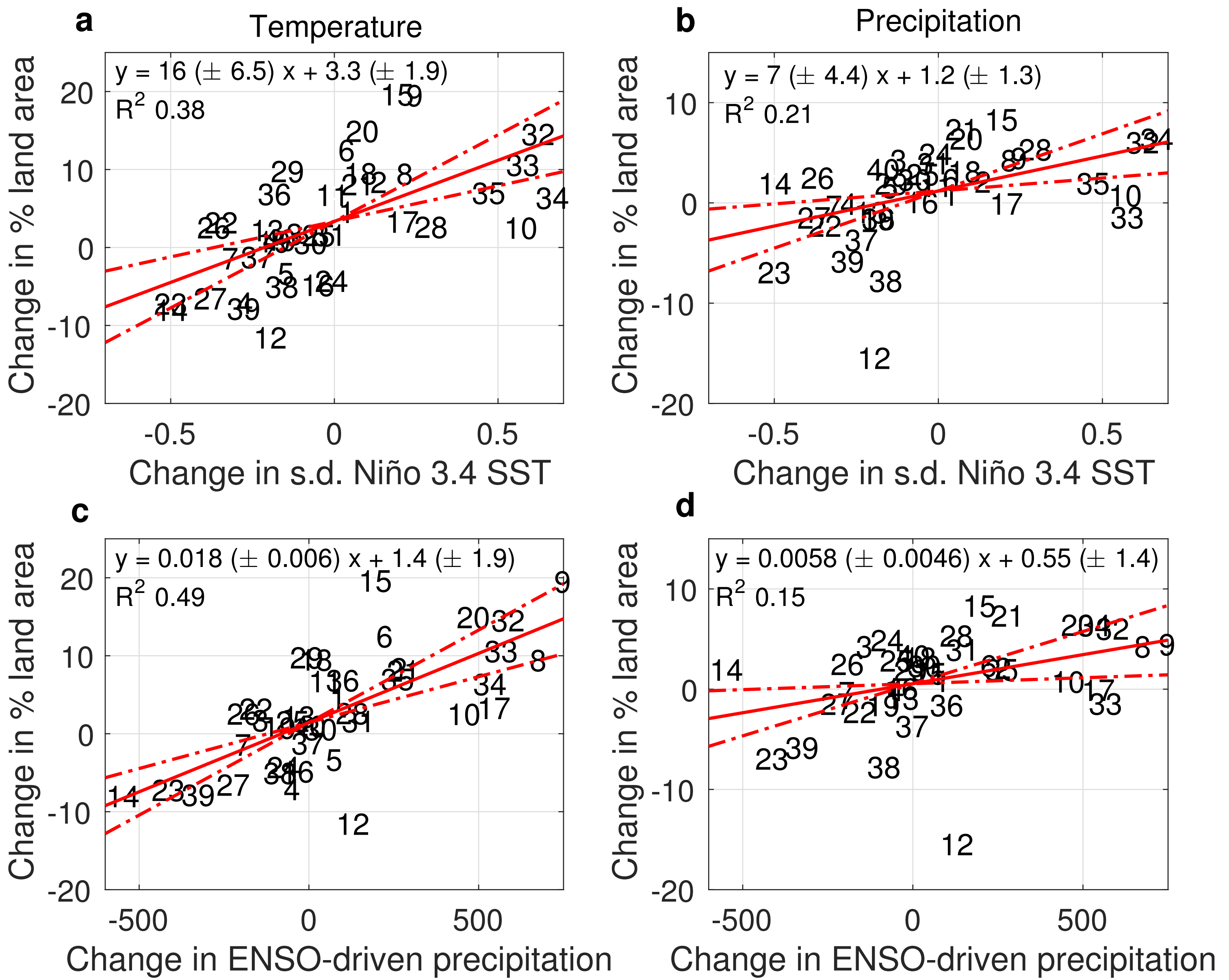
a
Temperature
y = 16 (± 6.5) x + 3.3 (± 1.9)
R2 0.38
Change in % land area
Change in s.d. Niño 3.4 SST
b
Precipitation
y = 7 (± 4.4) x + 1.2 (± 1.3)
R2 0.21
Change in % land area
Change in s.d. Niño 3.4 SST
c
y = 0.018 (± 0.006) x + 1.4 (± 1.9)
R2 0.49
Change in % land area
Change in ENSO-driven precipitation
d
y = 0.0058 (± 0.0046) x + 0.55 (± 1.4)
R2 0.15
Change in % land area
Change in ENSO-driven precipitation

Figure 4.

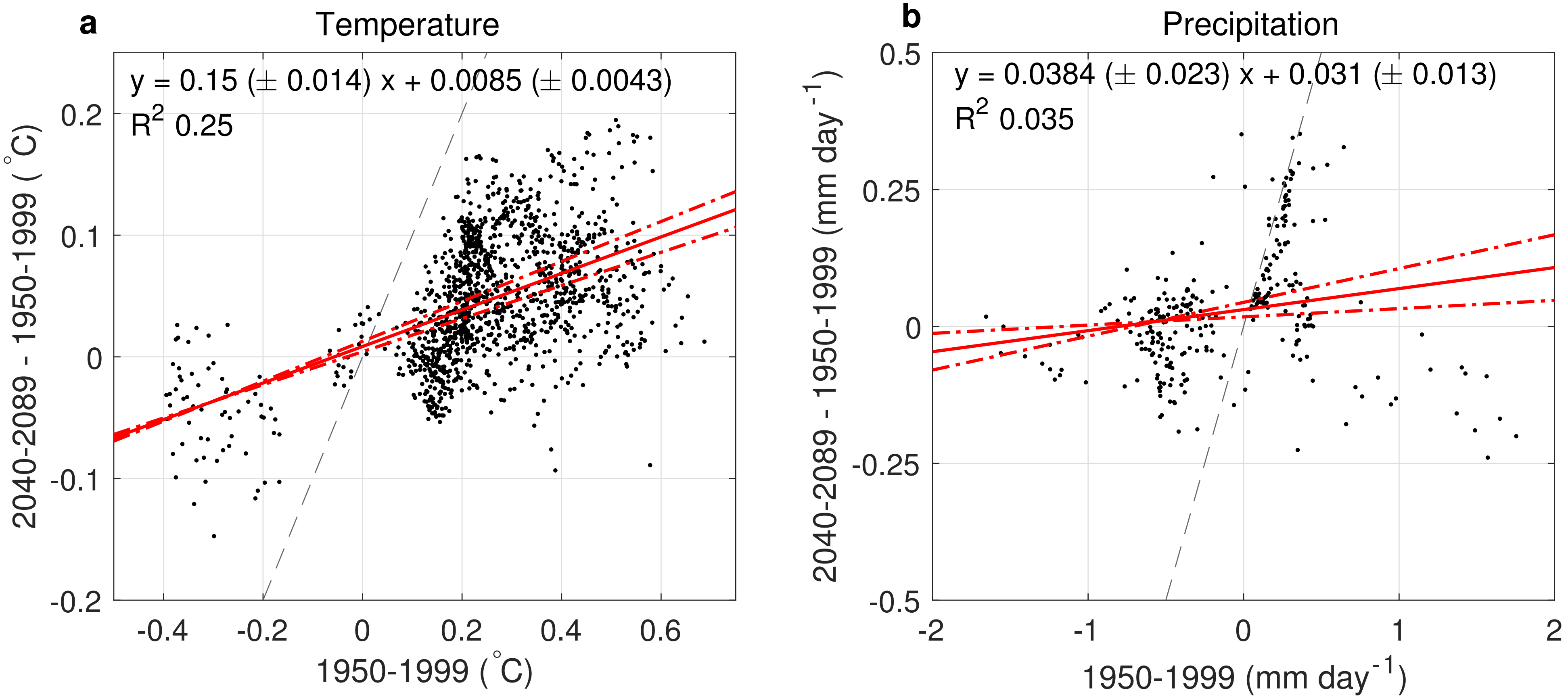

a
Temperature
y = 0.15 (± 0.014) x + 0.0085 (± 0.0043)
R2 0.25
0.2
0.1
0
-0.1
-0.2
2040-2089 - 1950-1999 (°C)
-0.4
-0.2
0
0.2
0.4
0.6
1950-1999 (°C)
b
Precipitation
y = 0.0384 (± 0.023) x + 0.031 (± 0.013)
R2 0.035
0.5
0.25
0
-0.25
-0.5
2040-2089 - 1950-1999 (mm day-1)
-2
-1
0
1
2
1950-1999 (mm day-1)